A cell-integrated semi-Lagrangian semi-implicit shallow-water model (CSLAM-SW) with conservative and consistent transport

MAY WONG *

University of British Columbia, Vancouver, British Columbia, Canada

WILLIAM C. SKAMAROCK, PETER H. LAURITZEN

National Center for Atmospheric Research,† Boulder, Colorado, USA

ROLAND B. STULL

University of British Columbia, Vancouver, British Columbia, Canada

* *Corresponding author address:* May Wong, University of British Columbia, 6339 Stores Road, Vancouver, BC Canada V6T 1Z4.

E-mail: mwong@eos.ubc.ca

†The National Center for Atmospheric Research is sponsored by the National Science Foundation.

ABSTRACT

A Cartesian semi-implicit solver using the conservative semi-Lagrangian transport scheme, CSLAM, is constructed and tested for shallow-water (SW) flows. The SW equations solver (CSLAM-SW) uses a discrete semi-implicit continuity equation specifically designed to ensure a conservative and consistent transport of constituents by avoiding the use of a constant mean reference state. The algorithm is constructed to be similar to typical conservative semi-Lagrangian semi-implicit schemes, requiring at each time step a single linear Helmholtz equation solution and a single application of CSLAM. The accuracy and stability of the solver is tested using four test cases for a radially-propagating gravity wave and two barotropically-unstable jets. In a consistency test using the new solver, the specific concentration constancy is preserved up to machine roundoff, whereas a typical formulation can have errors many orders of magnitude larger. In addition to mass-conservation and consistency, CSLAM-SW also ensures shape-preservation by combining the new scheme with existing shape-preserving filters. With promising SW test results, CSLAM-SW shows potential for extension to a non-hydrostatic, fully-compressible system solver for numerical weather prediction and climate models.

1. Introduction

Semi-Lagrangian semi-implicit (SLSI) schemes have been widely used in climate and numerical weather prediction (NWP) models since the pioneering work of Robert (1981) and Robert et al. (1985). The more lenient numerical stability condition in these schemes allows larger time steps and thus increased computational efficiency. Traditional semi-Lagrangian schemes are not inherently mass-conserving due to their use of grid-point interpolation, and the lack of conservation can lead to accumulation of significant solution errors (Rasch and Williamson 1990; Machenhauer and Olk 1997). To address this issue, conservative semi-Lagrangian schemes, also called cell-integrated semi-Lagrangian (CISL) transport schemes (Rancic 1992; Laprise and Plante 1995; Machenhauer and Olk 1997; Zerroukat et al. 2002; Nair and Machenhauer 2002; Lauritzen et al. 2010), have been developed. Although CISL transport schemes allow for locally (and thus globally) conservative transport of total fluid mass and constituent (i.e. tracer) mass, an issue related to conservation remains when they are applied in fluid flow solvers: the lack of consistency between the numerical representation of the total mass continuity and constituent mass conservation equations (Jöckel et al. 2001; Zhang et al. 2008). The lack of numerical consistency between the two can lead to the unphysical generation or removal of model constituent mass, which can introduce significant errors in applications such as chemical tracer transport (Machenhauer et al. 2009).

Our testbed for developing and testing CISL-based fluid flow solvers are the shallow-water (SW) equations on an f-plane:

$$\frac{\partial u}{\partial t} + u\frac{\partial u}{\partial x} + v\frac{\partial u}{\partial y} - fv - g'\frac{\partial h}{\partial x} = 0, \tag{1}$$

$$\frac{\partial v}{\partial t} + u\frac{\partial v}{\partial x} + v\frac{\partial v}{\partial y} + fu - g'\frac{\partial h}{\partial y} = 0, \tag{2}$$

$$\frac{\partial h}{\partial t} + \nabla \cdot (h\mathbf{v}) = 0, \tag{3}$$

$$\frac{\partial (hq)}{\partial t} + \nabla \cdot (hq\mathbf{v}) = 0 \tag{4}$$

where $\mathbf{v} = (u, v)$ is the horizontal velocity vector, f is the Coriolis parameter, g' is the reduced gravity, h is the total fluid depth (a surrogate for total fluid mass), and hq is the depth portion (mass fraction) of an arbitrary constituent, where q is its specific concentration. Numerical consistency is satisifed if, for $q_0 = 1$, the discretization scheme of the constituent equation (4) collapses to that for the continuity equation (3), also known as free-stream preservation.

The difficulty in maintaining consistency, as will be discussed in more detail, can partly be attributed to the conventional linearization around a constant mean reference state in the semi-implicit form of a CISL continuity equation. To eliminate the reference state, Thuburn (2008) developed a fully-implicit CISL-based scheme for the shallow-water equations that requires solving a nonlinear Helmholtz equation at every time step. The solution of the Helmholtz equation is potentially problematic and expensive (Thuburn et al. 2010). To reduce the dependence of their semi-implicit scheme on a reference state, Thuburn et al. (2010) used an alternative iterative approach to solve the nonlinear system, but it requires multiple calls to a Helmholtz solver per time step, again making the scheme potentially expensive.

In addition to consistency and mass conservation, another desirable property is that the new scheme should be shape-preserving. A shape-preserving scheme ensures that no new unphysical extrema are generated in a field due to the numerical scheme (e.g. Machenhauer et al. 2009). For example, specific concentrations of a passive constituent should not go outside the range of its initial minimum and maximum values. Non-shape-preserving schemes may generate unphysical specific concentrations, such as negative concentration values due to undershooting.

In this paper, using a shallow-water system, we present a new SLSI formulation that uses a CISL scheme for mass conservation and ensures numerical consistency between the total mass and constituent-mass fields. The new scheme is based on the CISL transport scheme called the Conservative Semi-LAgrangian Multi-tracer transport scheme (CSLAM) developed by

Lauritzen et al. (2010). Like other typical conservative SLSI solvers, the algorithm requires a single linear Helmholtz equation solution and a single application of CSLAM. To ensure shape-preservation, the scheme is further extended to use existing shape-preserving filters.

The paper is organized as follows. In section 2, the conservative semi-Lagrangian scheme CSLAM is described and a discussion of the issue of consistency between total-mass and constituent-mass conservation in its semi-implicit formulation is provided. A new consistent semi-implicit discretization of the CSLAM continuity equation, including the implementation of the shape-preserving schemes, is proposed in section 3. Results from four test cases are presented in section 4, highlighting the stability and accuracy of the new scheme for linear and highly-nonlinear flows, as well as showing the shape-preserving ability of the scheme. And finally, in section 5, a summary of the results and a potential extension of the new scheme are given.

2. Mass conservation and consistency in SLSI solvers

a. CSLAM — a CISL transport scheme

The CSLAM transport scheme is a backward-in-time CISL scheme, where the departure grid cell area δA^* is found by tracing the regular arrival grid cell area ΔA back in time one time-step Δt (Fig. 1a). The CSLAM discretization scheme for (3) is given by

$$h_{\text{exp}}^{n+1}\Delta A = h_*^n \delta A^*$$

where the superscript denotes the time level, h_{exp}^{n+1} is the explicit cell-averaged height solution computed by integrating the height field h^n over δA^*, which gives departure cell-averaged height values h_*^n. The departure cell area δA^* in CSLAM is found through iterative trajectory computations from the four vertices of an arrival grid cell (unfilled circles in Fig. 1b) to their departure points (filled circles in Fig. 1b). The departure cell area is then approximated using straight lines as cell edges (dark grey region δA in Fig. 1b). To integrate the height field over δA, CSLAM implements a remapping algorithm that consists of a piecewise biparabolic sub-grid-cell reconstruction of the h^n field, and then the integration of the reconstruction function over the departure cell area. The area integration in CSLAM is transformed into a series of line integrals using the Gauss-Green theorem, and involves solving for a set of weights that depends only on the departure cell boundary. The use of line integrals greatly enhances the transport scheme's computational efficiency for multi-tracer transport as the weights can be reused for all tracer species in the model. For full details on the transport scheme, see Lauritzen et al. (2010).

b. A discrete semi-implicit continuity equation in velocity-divergence form using CSLAM

Lauritzen et al. (2006) (which we will refer to as LKM) developed an SLSI SW equations solver using the explicit CISL transport scheme of Nair and Machenhauer (2002). For the momentum equations (1) and (2), they used a traditional SLSI discretization ((A1) and (A2) in the Appendix but without time-off-centering). Their momentum equations are then implicitly coupled to a velocity divergence correction term in the continuity equation. In this paper we follow the construction of the SW equations solver described in LKM, but we use CSLAM as the explicit CISL transport scheme. The discrete semi-implicit CISL continuity equation given in LKM (eq.(31) in LKM) is

$$\begin{aligned} h^{n+1} = h^{n+1}_{\text{exp}} &- \frac{\Delta t}{2} H_0 \left[\nabla_{\text{eul}} \cdot \mathbf{v}^{n+1} - \nabla_{\text{lag}} \cdot \tilde{\mathbf{v}}^{n+1} \right] \\ &+ \frac{\Delta t}{2} H_0 \overline{\left[\nabla_{\text{eul}} \cdot \mathbf{v}^{n} - \nabla_{\text{lag}} \cdot \mathbf{v}^{n} \right]} \frac{\delta A^*}{\Delta A}, \end{aligned} \tag{5}$$

where h^{n+1}_{exp} is as described above, Δt is the model time step, H_0 is the constant mean reference height, $\mathbf{v}^{n+1}$ is the velocity field implicitly coupled to the momentum equations, $\tilde{\mathbf{v}}^{n+1} = 2\mathbf{v}^n - \mathbf{v}^{n-1}$ is the velocity field extrapolated to time-level $n+1$, and $\mathbf{v}^n$ is the velocity field at time-level n. Their semi-implicit correction term (first term in brackets in (5)) is the correction to the explicit solution h^{n+1}_{exp} from the CSLAM scheme, and the second term in brackets in (5) is a predictor-corrector term (where the overbar denotes the departure cell-averaged value). The implicit linear terms are obtained, as in the traditional approach (e.g., Kwizak and Robert (1971); Machenhauer and Olk (1997)), by linearizing the height field around a constant mean reference state, and hence (5) results in a velocity-divergence form. The notations ∇_{eul} and ∇_{lag} denote discretized divergence operators based on the Eulerian and Lagrangian forms respectively. Using notations in Fig. 2, the Eulerian divergence operator is given by

$$\nabla_{\text{eul}} \cdot \mathbf{v} = \frac{1}{\Delta x}(u_r - u_l) + \frac{1}{\Delta y}(v_t - v_b).$$

The Lagrangian divergence operator (eq.(25) in LKM) is given by

$$\nabla_{\text{lag}} \cdot \mathbf{v} = \frac{1}{\Delta A}\frac{\Delta A - \delta A}{\Delta t}, \tag{6}$$

and is computed as the change in cell area in one time step.

The form of the semi-implicit correction term in (5) is due to the split-divergence approximation (eq. (26) in LKM)

$$\nabla \cdot \mathbf{v}^{n+1/2} \approx \frac{1}{2}\Big[\nabla \cdot \tilde{\mathbf{v}}^{n+1} + \nabla \cdot \mathbf{v}^{n}\Big]$$

applied to the linearized divergence term of the semi-implicit continuity equation. The split-divergence approximation is used to evaluate the linear divergence term at the mid-point trajectory (at time-level $n+1/2$). As explained in Lauritzen et al. (2006), this approximation stems from their trajectory algorithm, where the trajectory is approximated as two segments: (i) from the departure point to the trajectory mid-point (computed iteratively), and (ii) from the mid-point to the arrival grid point (computed using extrapolated winds; see Fig. 1 in LKM). Since the Lagrangian divergence is calculated based on the change of cell area over time, and departure cell areas are computed using the split-trajectory algorithm, the split-approximation can also be applied to the divergence term (Lauritzen et al. 2006).

Ideally, to be consistent, the implicit and the extrapolated divergences would both be solved in a Lagrangian fashion; however, this would lead to a nonlinear elliptic equation instead of a standard Helmholtz equation (Lauritzen 2005). To retain a linear elliptic equation, Lauritzen et al. (2006) implemented a predictor-corrector approach to correct for the Eulerian discretization of the implicit divergence term, and found that this step was necessary to maintain stability in their model. In our implementation of the LKM solver using CSLAM, we follow the approach of Lauritzen et al. (2006), where the predictor-corrector term (second term in brackets in (5)) is evaluated by integrating the departure cell-averaged value over δA^*.

c. Numerical inconsistency in semi-implicit continuity equations in a velocity-divergence form

Numerical consistency between total mass and constituent mass is difficult to maintain in semi-implicit CISL schemes such as LKM. The prognostic constituent mass variable hq is typically solved explicitly using

$$hq^{n+1} = hq^{n+1}_{\mathrm{exp}}, \tag{7}$$

where hq^{n+1}_{exp} is the CISL explicit solution, h is the shallow-water height (analogous to total air mass in a full model), and q is the specific concentration of an arbitrary constituent. The cell-integrated transport equation in its flux-form helps conserve constituent mass, analogous to the amount of water vapour and other passive tracers in an atmospheric model — an important constraint especially for long simulations. Since the departure cell areas are the same for both total fluid mass and the constituent mass, the weights of the line integrals in CSLAM will need to be computed only once per time step, and represents one of the advantages of this scheme.

If the discrete constituent equation is consistent with the discrete continuity equation, the former should reduce to the latter when $q = 1$, and an initially spatially uniform specific concentration field should remain so. For a divergent flow, however, the semi-implicit correction term in (5) may become large enough such that (7), in its explicit form, is no longer consistent (Lauritzen et al. 2008).

Alternatively, one can formulate the discrete constituent equation by including the semi-implicit correction and predictor-corrector terms in (5) to maintain numerical consistency between the two equations, i.e.

$$
\begin{aligned}
hq^{n+1} = hq^{n+1}_{\mathrm{exp}} &- \frac{\Delta t}{2} HQ_0 \left[\nabla_{\mathrm{eul}} \cdot \mathbf{v}^{n+1} - \nabla_{\mathrm{lag}} \cdot \tilde{\mathbf{v}}^{n+1} \right] \\
&+ \frac{\Delta t}{2} HQ_0 \overline{\left[\nabla_{\mathrm{eul}} \cdot \mathbf{v}^{n} - \nabla_{\mathrm{lag}} \cdot \mathbf{v}^{n} \right]} \frac{\delta A^*}{\Delta A},
\end{aligned} \tag{8}
$$

where HQ_0 is a constant mean reference constituent mass, the velocities $\mathbf{v}^{n+1}$ are solutions from the Helmholtz solver, and $\tilde{\mathbf{v}}^{n+1}$ and $\mathbf{v}^n$ are the same velocities as in (5).

However, the dependence on a constant mean reference constituent mass HQ_0 may create a source of numerical errors for regions with little constituent mass. For example, in regions where $hq^{n+1}_{\mathrm{exp}} = 0$, if the flow is highly-divergent such that the terms in square brackets in (8) are non-zero, spurious constituent mass will be erroneously generated due to a non-zero constant mean constituent mass. Similarly, in areas where hq^{n+1}_{exp} is a non-zero constant, spurious deviation from constancy can be generated by the correction terms.

The issue with an inconsistent constant mean reference state for the total fluid mass and constituent mass fields can be resolved with the formulation we present in the next section.

3. A consistent and mass-conserving semi-implicit SW solver

Our new scheme ensures numerical consistency between the continuity and constituent equations by formulating the discrete equations, specifically the semi-implicit correction and the predictor-corrector terms, in flux form instead of a velocity-divergence form. The goal is to avoid the use of a constant reference state, such as (5). We test this approach for the SW equations, and refer to the model using the flux-form scheme as CSLAM-SW. We formulate the semi-implicit flux-form continuity equation as

$$
\begin{aligned}
h^{n+1} = h_{\mathrm{exp}}^{n+1} &- \frac{\Delta t}{2}\Big[\nabla_{\mathrm{eul}} \cdot (h_{\mathrm{exp}}^{n+1}\mathbf{v}^{n+1}) - \nabla_{\mathrm{lag}} \cdot (h_{\mathrm{exp}}^{n+1}\tilde{\mathbf{v}}^{n+1})\Big] \\
&+ \frac{\Delta t}{2}\overline{\Big[\nabla_{\mathrm{eul}} \cdot (h^n\mathbf{v}^n) - \nabla_{\mathrm{lag}} \cdot (h^n\mathbf{v}^n)\Big]}\frac{\delta A^*}{\Delta A},
\end{aligned}
\tag{9}
$$

and use the explicit CSLAM solution h_{exp}^{n+1} as the reference state in the semi-implicit correction term. The shallow-water model CSLAM-SW, like the LKM model, couples the semi-implicit height continuity equation with the traditional semi-Lagrangian momentum equations, as described in the Appendix, and solves the resulting elliptic system with a conjugate-gradient Helmholtz solver.

To ensure consistency, we simply express the constituent equation as

$$
\begin{aligned}
hq^{n+1} = hq_{\mathrm{exp}}^{n+1} &- \frac{\Delta t}{2}\Big[\nabla_{\mathrm{eul}} \cdot (hq_{\mathrm{exp}}^{n+1}\mathbf{v}^{n+1}) - \nabla_{\mathrm{lag}} \cdot (hq_{\mathrm{exp}}^{n+1}\tilde{\mathbf{v}}^{n+1})\Big] \\
&+ \frac{\Delta t}{2}\overline{\Big[\nabla_{\mathrm{eul}} \cdot (hq^n\mathbf{v}^n - \nabla_{\mathrm{lag}} \cdot (hq^n\mathbf{v}^n)\Big]}\frac{\delta A^*}{\Delta A},
\end{aligned}
\tag{10}
$$

where hq_{exp}^{n+1} is the explicit CSLAM update to the constituent mass, the velocities $\mathbf{v}^{n+1}$ in $\nabla_{\mathrm{eul}} \cdot (hq_{\mathrm{exp}}^{n+1}\mathbf{v}^{n+1})$ are from the SLSI solution, and hq^n and $\mathbf{v}^{\mathbf{n}}$ are the constituent mass and velocity at time-level n respectively. This scheme also resolves the problem of spurious generation of constituent mass for regions with near-zero specific concentration (as described in the previous section). The specific concentration q is diagnosed by decoupling the constituent mass using

$$
q^{n+1} = \frac{hq^{n+1}}{h^{n+1}}. \tag{11}
$$

We note that to ensure numerical consistency, we must eliminate machine-roundoff and convergence errors in the Helmholtz solver. In solving for hq^{n+1}, we substitute the solutions of $\mathbf{v}^{n+1}$ derived from the Helmholtz solution h^{n+1} into (10). Prior to diagnosing q using (11), we must correct the solution h^{n+1} by substituting solutions of $\mathbf{v}^{n+1}$ back into (9); otherwise, the values of h^{n+1} can become inconsistent with hq^{n+1}. The consistent h^{n+1} solution is then used to solve for q using (11) and in the next time step. To compute hq_{exp}^{n+1}, we follow Nair and Lauritzen (2010) in separating the sub-grid-cell reconstructions for h and q, and then compute $hq(x,y)$ using

$$hq(x,y) = \overline{h}q + \overline{q}(h - \overline{h}),$$

where $h = h(x,y)$ and $q = q(x,y)$ are the reconstruction functions, and $(\overline{h}, \overline{q})$ are cell averages.

The new flux-form conservation equations (9) and (10) involve the computation of an Eulerian flux-divergence and a Lagrangian flux-divergence using extrapolated velocities. Using the mesh described in Fig. 2, the discrete Eulerian flux-divergence is given as

$$\nabla_{\text{eul}} \cdot (h\mathbf{v}) = \frac{1}{\Delta x}\Big[(\overline{h}^x u)_r - (\overline{h}^x u)_l\Big] + \frac{1}{\Delta y}\Big[(\overline{h}^y v)_t - (\overline{h}^y v)_b\Big], \tag{12}$$

where Δx and Δy are the grid spacing in the x- and y-directions, and each of the fluxes are evaluated as $\overline{h}^x_r u_r$, $\overline{h}^x_l u_l$, $\overline{h}^y_t v_t$, and $\overline{h}^y_b v_b$ respectively.

The Lagrangian flux-divergence in (10) needs to be consistent with the Lagrangian velocity-divergence (6). To derive the new operator, we begin by computing the Lagrangian backward-trajectories of the arrival grid cell vertices given in Fig. 2. We define the arrival cell corner points to be at $(\vec{x}_1,\ \vec{x}_2,\ \vec{x}_3,\ \vec{x}_4)$, i.e. (x_1, y_1), (x_2, y_2), (x_3, y_3), (x_4, y_4), and the departure cell corner points as

$$\begin{aligned}
\vec{x}_{d1} &= \vec{x}_1 - \Delta t \cdot (u_c,\ v_c)_1, \\
\vec{x}_{d2} &= \vec{x}_2 - \Delta t \cdot (u_c,\ v_c)_2, \\
\vec{x}_{d3} &= \vec{x}_3 - \Delta t \cdot (u_c,\ v_c)_3, \\
\vec{x}_{d4} &= \vec{x}_4 - \Delta t \cdot (u_c,\ v_c)_4,
\end{aligned}$$

where $(u_c, v_c)_i = (\overline{u}^y, \overline{v}^x)_i$ denote the x- and y-velocity components at the i^{th} vertex, where $i = 1, 2, 3, 4$.

The area of the departure cell is computed as

$$\delta A = \frac{1}{2}\Big[\vec{x}_{d21} \times \vec{x}_{d41} + \vec{x}_{d43} \times \vec{x}_{d23}\Big],$$

where $\vec{x}_{d21} = \vec{x}_{d2} - \vec{x}_{d1}$; $\vec{x}_{d41} = \vec{x}_{d4} - \vec{x}_{d1}$; $\vec{x}_{d43} = \vec{x}_{d4} - \vec{x}_{d3}$; and $\vec{x}_{d23} = \vec{x}_{d2} - \vec{x}_{d3}$. We can then rewrite the departure cell area as

$$\delta A = \Delta x \Delta y - \Delta t \Big[\mathcal{F}_r - \mathcal{F}_l + \mathcal{F}_t - \mathcal{F}_b \Big]. \tag{17}$$

where

$$\mathcal{F}_r = \overline{u_r}^{yy} \Delta y - (u_{c2} v_{c3} - u_{c3} v_{c2}) \Delta t / 2,$$

$$\mathcal{F}_l = \overline{u_l}^{yy} \Delta y - (u_{c1} v_{c4} - u_{c4} v_{c1}) \Delta t / 2,$$

$$\mathcal{F}_t = \overline{v_t}^{xx} \Delta x - (u_{c3} v_{c4} - u_{c4} v_{c3}) \Delta t / 2,$$

$$\mathcal{F}_b = \overline{v_b}^{xx} \Delta x - (u_{c2} v_{c1} - u_{c1} v_{c2}) \Delta t / 2.$$

Using (17), the velocity divergence can be written as:

$$\mathbb{D} = \frac{1}{\Delta x \Delta y} \Big[\mathcal{F}_r - \mathcal{F}_l + \mathcal{F}_t - \mathcal{F}_b \Big],$$

which is identical to the Lagrangian divergence (6). The first flux term in each of $\mathcal{F}_r$, $\mathcal{F}_l$, $\mathcal{F}_t$, and $\mathcal{F}_b$ is identical to the Eulerian velocity-divergence and the remaining terms give the geometric correction for a Lagrangian representation (see Fig. 9 in Lauritzen 2005). Using this velocity divergence, we now approximate the Lagrangian flux-divergence term in equation (9) as:

$$\nabla_{\text{lag}} \cdot (h\mathbf{v}) = \frac{1}{\Delta x \Delta y} \Big[\mathcal{F}_r \overline{h}_r^x - \mathcal{F}_l \overline{h}_l^x + \mathcal{F}_t \overline{h}_t^y - \mathcal{F}_b \overline{h}_b^y \Big]. \tag{18}$$

Using (12) and (18) and replacing h with hq, we can further combine each of the terms in brackets of the constituent equation (10), which becomes

$$\begin{aligned} hq^{n+1} = hq^{n+1}_{\text{exp}} &- \frac{\Delta t}{2} \Big[\nabla_{\text{eul}} \cdot (h^{n+1}_{\text{exp}} q^{n+1*}_{\text{exp}} \mathbf{v}'^{n+1}) \Big] \\ &+ \frac{\Delta t}{2} \overline{\Big[\nabla_{\text{eul}} \cdot (h^n q^{n*} \mathbf{v}'^n) \Big]} \frac{\delta A^*}{\Delta A}, \end{aligned} \tag{19}$$

where

$$\nabla_{\text{eul}} \cdot (hq^* \mathbf{v}') = \frac{1}{\Delta x} \left[\overline{h}_r^x \overline{q^*}_r^x (u_r - \mathcal{F}_r/\Delta y) - \overline{h}_l^x \overline{q^*}_l^x (u_l - \mathcal{F}_l/\Delta y) \right] + \frac{1}{\Delta y} \left[\overline{h}_t^y \overline{q^*}_t^y (v_t - \mathcal{F}_t/\Delta x) - \overline{h}_b^y \overline{q^*}_b^y (v_b - \mathcal{F}_b/\Delta x) \right].$$

The corrective velocity $\mathbf{v}'$ is defined as the difference between the velocity field used in the Eulerian flux divergence (12) and that derived from the Lagrangian flux areas $\mathcal{F}_r$, $\mathcal{F}_l$, $\mathcal{F}_t$, and $\mathcal{F}_b$, divided by the cell face length. The corrective velocity $\mathbf{v}'^{n+1}$ in (19) is computed using $\mathbf{v}^{n+1}$ from the Helmholtz solver and the Lagrangian flux areas based on extrapolated winds divided by the cell face length. The velocity $\mathbf{v}'^n$ used in the predictor-corrector term in (19) is computed using the velocity field $\mathbf{v}^n$ at time-level n and the Lagrangian flux areas based on $\mathbf{v}^n$, and again divided by the cell face length. Shape-preserving schemes, e.g. the first-order upwind scheme, or higher-order methods such as flux-corrected transport schemes or flux-limiter schemes, can then be applied to the fluxes in (19). The first-order upwind scheme is used here, where the upstream values (denoted by the asterisks) q_{exp}^{n+1*} and q^{n*} at each cell face are determined by the directions of $\mathbf{v}'^{n+1}$ and $-\mathbf{v}'^n$ respectively (see e.g. Durran 2010, eq.(5.109)). The first-order upwind scheme is numerically diffusive (Durran 2010), but the damping effect on the correction and predictor-corrector terms should be minimal as the corrective velocities $\mathbf{v}'^{n+1}$ and $\mathbf{v}'^n$ are typically very small. To ensure shape-preservation in the explicit CSLAM solution, we implement a simple 2D monotonic filter (Barth and Jespersen 1989) that searches for new local minima and maxima in the reconstruction function of q, and scales the function if these values exceed those in the neighbouring cell.

Testing of the CSLAM-SW model [based on (9) for h, and (A1) and (A2) for the velocity components] revealed an instability related to the averaging of the C-grid velocities to the cell corner points in the continuity equation and its interaction with the rotational modes. Following Randall (1994), we can write a generalized discretized dispersion relation for the linearized shallow-water equations as

$$\omega^3 - \omega(c^2 l_v l_h + c^2 k_u k_h + f_u f_v) - ic^2(f_u k_h l_v - f_v k_u l_h) = 0, \tag{20}$$

where the terms f_u and f_v are the discrete Coriolis operators, k_u and l_v are the discrete height-gradient operators, k_h and l_h are the discrete velocity-divergence operators in the continuity equation (the letter subscripts refer to the equations in which they appear), and $c^2 = gH$. In the linearized shallow-water dispersion relation for C-grid, the last two terms on the L.H.S. of (20), $f_u k_h l_v$ and $f_v k_u l_h$, cancel and thus there are no numerical frequencies ω with imaginary parts that amplify in time. Although the CSLAM-SW model uses the C-grid, we have found that the discretization of the linearized Lagrangian divergence is equivalent to taking an average of the u and v velocities to the corners of the grid cell followed by an averaging back to the cell-faces, i.e. the discretization is equivalent to using a 1-2-1-averaging of the u velocities in the y-direction, and of the v velocities in the x-direction, at the Eulerian grid cell faces. This averaging leads to non-cancellation of $f_u k_h l_v$ and $f_v k_u l_h$, and growing modes. We have found that using the averaging operators $\overline{\overline{v}^{xy}}^{xx}$ and $\overline{\overline{u}^{xy}}^{yy}$ (see Appendix for operator definitions) on the Coriolis terms in the x- and y-momentum equations, respectively, recovers the cancellation and eliminates the unstable mode.

4. Test cases

We present four test problems involving divergent flows: a radially-propagating gravity wave (with two different initial perturbations), and two highly-nonlinear barotropically unstable jets (the Bickley and the Gaussian jets from Poulin and Flierl (2003)). The gravity-wave problem (section 4a) is a simple case to assess the stability and accuracy of the new SLSI solver (CSLAM-SW) with respect to an imposed mean flow speed and the gravity-wave propagation speed. We also use this test case to highlight the issue of numerical inconsistency in the constituent transport scheme of LKM. The nonlinearity of the unstable jet in the second problem is particularly useful in testing the stability limits of the new scheme. The

Bickley jet (section 4b) has a moderate gradient in the initial height profile, while the steeper profile in the Gaussian jet (section 4c) drives a more unstable jet. These strong gradients provide a severe test for advection schemes. In addition to those from LKM, solutions from a traditional semi-Lagrangian formulation and an Eulerian formulation (see Appendix) are also presented for comparison. We use the highly-divergent Gaussian jet case to compare the solutions between the shape-preserving CSLAM-SW solver described by (19) and the LKM with a shape-preserving explicit transport scheme (section 4d).

a. A radially-propagating gravity wave

A non-rotating ($f = 0$) 2D radially-propagating gravity wave is initiated by a circular height perturbation h' and advected by a mean background flow:

$$u(x, y, t = 0) = u_0 = 1.2 \text{ m s}^{-1},$$
$$v(x, y, t = 0) = v_0 = 0.9 \text{ m s}^{-1},$$
$$h(x, y, t = 0) = h_0 + h',$$

where

$$h' = \begin{cases} \frac{1}{2}\Delta h\left[1 + \cos\left(\frac{\pi r}{10 \text{ km}}\right)\right], & \text{if } r \leq 10 \text{ km}, \\ 0, & \text{otherwise}, \end{cases}$$

and h_0 is the initial background height, Δh is the magnitude of the initial height perturbation, $r = \sqrt{(x - x_c)^2 + (y - y_c)^2}$, and (x_c, y_c) is the center of a 200 km $\times$ 200 km domain. We perform tests for two different initial height perturbations: a linear case with $\Delta h = 10$ m and $h_0 = 990$ m; and a nonlinear case with $\Delta h = 500$ m and $h_0 = 1000$ m. A reduced gravitational acceleration of $g' \approx 0.0204$ m s^{-2} is used, giving an initial gravity wave speed $c = \sqrt{g'h}$ of 4.5 m s^{-1} and 5.5 m s^{-1} for the two cases respectively. The mean advection speed $\left(\sqrt{u_0^2 + v_0^2} = 1.5 \text{ m s}^{-1}\right)$ is chosen to emulate the speed ratio of the fastest advection of sound waves (≈ 300 m s^{-1}) in the atmosphere to the speed of the jet stream (≈ 100 m s^{-1}). The background flow velocities $u_0 \neq v_0$ are also chosen to ensure that the flow does not align with the mesh.

The model domain consists of 400 $\times$ 400 grid cells, with a grid spacing of $\Delta x = \Delta y =$ 500 m, and is periodic in both x- and y-directions. Since there is no analytical solution to the test problem, to evaluate CSLAM-SW, we produce a fine-resolution Eulerian reference solution with a grid spacing of $\Delta x = \Delta y = 100$ m and a time step of $\Delta t = 10$ s. The center of the gravity wave disturbance in the reference solution is stationary (i.e. $u_0 = v_0 = 0$ m s^{-1}), and we compare the solutions by translating the gravity wave disturbance in CSLAM-SW to the center of the domain.

In addition to CSLAM-SW, we also run the two initial perturbation cases using LKM, the traditional semi-Lagrangian formulation, and an Eulerian formulation. We use the l_2-norm of error as the error measure, which for a uniform mesh is

$$l_2 = \frac{\sqrt{\sum_{i,j} \left[h(i,j) - h_{\text{ref}}(i,j)\right]^2}}{\sqrt{\sum_{i,j} \left[h_{\text{ref}}(i,j)\right]^2}},$$

where i, j are the grid indices, $h(i,j)$ is the model solution, and $h_{\text{ref}}(i,j)$ is the Eulerian high-resolution reference solution. The l_2-norm of error in the height field (at time $T = 1 \times 10^5$ s) for different time step sizes is shown in Fig. 3 for all four models. Results from both the linear and nonlinear initial perturbations are plotted. The time truncation error in CSLAM-SW is very comparable to those in the other two semi-Lagrangian models for both cases. Except for the Eulerian model, all model solutions converge as the time step size is reduced to less than $\Delta t = 50$ s. At this point, differences between the errors are mainly due to the spatial discretization schemes (more noticeably in the nonlinear case). The Eulerian model and the traditional semi-Lagrangian model have a commonality that they both use a 'true' C-grid divergence operator in the continuity equation; whereas as discussed in Section 3, the CISL computation of divergence in both CSLAM-SW and LKM consists of an extra averaging operator. For this reason, one may see a smaller spatial discretization error in the traditional semi-Lagrangian model and "coarse" Eulerian model when compared to an

Eulerian high-resolution reference solution than those in the CISL models, as is the case in Fig. 3.

To evaluate the consistency in CSLAM-SW and LKM, a constituent with an initially constant specific concentration distribution ($q_0 = 1$) is initialized in each model. The CSLAM explicit transport scheme conserves constituent mass in both models; however, as discussed in section 2c, when numerical consistency is violated, constancy of the specific concentration is not guaranteed, and generation or removal of constituent mass is possible. The specific concentration is diagnosed by decoupling the constituent mass variable using (11). A time step of $\Delta t = 100$ s is used. Fig. 4 shows an example of the specific concentration error in LKM at time $T = 1 \times 10^5$ s for both the linear and nonlinear perturbation cases. The error is largest near the leading edge of the gravity wave, where the flow is most divergent and the semi-implicit correction term is non-zero. Fig. 5 shows the variation in error with time step size for both the linear and nonlinear perturbations at the same simulation time as in Fig. 4. The error measures used are the maximum absolute error, the mean absolute error, and the root-mean-squared error. Errors in the solutions from LKM and CSLAM-SW are shown in solid and dashed lines respectively. Since the inconsistent semi-implicit correction in (5) is proportional to Δt, errors in the scalar field grow with time step size, which can become a major issue for semi-Lagrangian models that take advantage of larger stable time steps. For the nonlinear test, the maximum absolute error from LKM is in the order of 10^{-2} to 10^{-1}, and is significant for constituents like water vapour which has a typical mixing ratio of roughly 0.1% to 3% in air. On the other hand, CSLAM-SW using a consistent formulation is free-stream preserving (up to machine roundoff) for both cases and all time-step sizes tested.

b. Bickley jet – Ro = 0.1

The stability of CSLAM-SW is further evaluated with two perturbed jets; we begin with the Bickley jet from Poulin and Flierl (2003). The Bickley jet is simulated at the Rossby number, $\mathrm{Ro} = U/fL = 0.1$, where U is the flow velocity scale, f is the Coriolis parameter and L is the length scale of the jet width. We choose the Froude number, $\mathrm{Fr} = (fL)^2/g'H = 0.1$. The jet is characterized by greater heights to the left of the channel and dropping off to smaller heights to the right, geostrophically-balanced by a mean flow velocity down the channel (Fig. 6). A height perturbation is superimposed at the initial time, causing wave amplification and eventual breaking of the jet into vortices, and formation of a vortex street along the channel. These vortex streets consist of thin filaments of vorticity with strong horizontal velocity shear, making it a good test because it is challenging for all numerical schemes. A more detailed description of the evolution of these jets can be found in Poulin and Flierl (2003).

The initial geostrophically-balanced mean state (u_0, v_0, and h_0) and height perturbation h' of the Bickley jet is given by:

$$\begin{aligned} u(x, y, t = 0) &= u_0 = 0, \\ v(x, y, t = 0) &= v_0 = -\frac{g'\Delta h}{fa}\mathrm{sech}^2\left(\frac{x}{a}\right), \\ h(x, y, t = 0) &= h_0 + h', \end{aligned}$$

where

$$\begin{aligned} h_0 &= 100 - \Delta h \tanh\left(\frac{x}{a}\right), \\ h' &= 0.1\Delta h\, \mathrm{sech}^2\left(\frac{x}{a}\right) \sin\left(\frac{2\pi y}{Y} n\right). \end{aligned}$$

The parameter Δh is the maximum amplitude of the height perturbation and depends on Ro, g' is the gravitational acceleration, a is the jet width, Y is the length of the channel, and n is the wavenumber mode of the height perturbation. In our simulations, $L = a = 1 \times 10^5$ m, X (width of channel) $= Y = 2 \times 10^6$ m, $f = 1 \times 10^{-4}$ s^{-1}, and $g' = 10$ m s^{-2}. For the specified scale of the jet width and a flow with Fr $= 0.1$, the mean height of h_0 is 100 m. The amplitude of the height perturbation $\Delta h = 1$ m is determined by the scale of the initially geostrophically-balanced flow speed ($U \sim 1$ m s^{-1}) for Ro $= 0.1$. We choose the most unstable mode of wavenumber $n = 3$ (Poulin and Flierl 2003) for all of our jet simulations.

Each grid domain has 202 × 202 grid cells and a grid spacing of $\Delta x = \Delta y = 9950$ m, with solid boundary conditions at $x = -X/2$ and $x = X/2$ and periodic boundary conditions in y where $y \in [-Y/2, Y/2]$. A time step of $\Delta t = 2000$ s was used in all simulations. Based on the initial gravity-wave speed $c \approx 32$ m s^{-1} and initial flow speed $|v| = 1$ m s^{-1}, the Courant numbers are $\mathrm{Cr}_{\mathrm{gw}} = 6.4$ and $\mathrm{Cr}_{\mathrm{adv}} = 0.2$ respectively.

To maintain numerical stability in the Eulerian model, we implemented a second-order explicit diffusion term with a numerical viscosity parameter $\beta_x = \beta_y = \nu\Delta t/\Delta x^2 = 0.02$ (where ν is analogous to the physical viscosity). This value corresponds to the numerical Reynolds number, $\mathrm{Re} = UL/\nu = 10^2$, a factor of 10 smaller than that used in the forward-in-time Eulerian model of Poulin and Flierl (2003). Explicit diffusion was not applied to any of the semi-Lagrangian models because the schemes have sufficient inherent damping to maintain numerical stability. For the traditional semi-Lagrangian model, however, we found that time-off-centering in the semi-implicit scheme was needed to maintain stability.

Fig. 7 shows the solutions from CSLAM-SW and the three comparison models. Although the exact form of the initial height perturbation was not provided in Poulin and Flierl (2003), we were able to reproduce results very similar to theirs [cf. Fig. 4c of Poulin and Flierl (2003)]. The most noticeable difference among the different model solutions is in the shape and magnitude of the relative vorticity maxima and minima. CSLAM-SW showed very similar vortex shapes to those from LKM and TRAD-SL. The vortices in the Eulerian results are similar to those from the Eulerian model of Poulin and Flierl (2003). The difference between the Eulerian solution and the semi-Lagrangian solutions can be attributed to the inherent damping in the reconstruction step of the CISL schemes and the grid-point interpolation in the traditional semi-Lagrangian scheme.

c. *Gaussian jet – Ro = 5.0*

The third test case is the Gaussian jet with Ro = 5.0. Similar to the Bickley jet, the Gaussian jet has Fr = 0.1, and has an initially geostrophically-balanced mean-state with greater heights to the left of the channel and dropping off to smaller heights to the right (Fig. 6). The main difference between the two jets is that the Gaussian jet has a slightly steeper height profile at the center of the channel, and therefore, produces a more pronounced nonlinear flow, especially at larger Ro. The initial mean state and height perturbation for the Gaussian jet is given as:

$$u(x, y, t = 0) = u_0 = 0,$$
$$v(x, y, t = 0) = v_0 = -\frac{2g'\Delta h}{\sqrt{\pi} f a} \exp(-(x/a)^2),$$
$$h(x, y, t = 0) = h_0 + h',$$

where

$$h_0 = 100 - \Delta h \,\mathrm{erf}\Big(\frac{x}{a}\Big),$$
$$h' = 0.1\Delta h\Big(\frac{2}{\sqrt{\pi}} \exp(-(x/a)^2\Big) \sin\Big(\frac{2\pi y}{y_L} n\Big),$$

and the notation is as before. All the parameters remain the same, except $\Delta h = 50$ m for Ro = 5.0, and $\Delta t = 100$ s is used. With an initial gravity-wave speed and maximum flow speed of 38 m s^{-1} and 56 m s^{-1} respectively, $\mathrm{Cr_{gw}} = 0.4$ and $\mathrm{Cr_{adv}} = 0.56$. We note that $U > c$, i.e. the flow is supercritical. Despite the existence of supersonic waves in the solution, CSLAM-SW is stable even at larger Courant numbers.

As pointed out in Poulin and Flierl (2003), jets in this Rossby regime are highly unstable and of particular interest is the formation of an asymmetric vortex street with triangular cyclones and elliptical anticyclones. As the vortex street is advected towards the deeper water, a strong cut-off cyclone develops due to vortex stretching (adjacent to the main anticyclonic feature). All of our models, including CSLAM-SW, were able to reproduce these features [Fig. 8, cf. Fig. 10e of Poulin and Flierl (2003)]. As in the Bickley jet case, we find that CSLAM-SW produced solutions similar to the other two semi-Lagrangian models (LKM and TRAD-SL).

In addition to comparing solutions of CSLAM-SW at time steps allowable by the Eulerian scheme, we also tested the stability of CSLAM-SW at a much larger $\mathrm{Cr_{adv}} = 2.5$. Figs. 9a-c show solutions at various times from the previous CSLAM-SW simulation ($\mathrm{Cr_{adv}} = 0.56$), and Figs. 9d-f show solutions at each of the corresponding time for $\mathrm{Cr_{adv}} = 2.5$, using the largest time step allowable by the Lipschitz condition for this flow. The solution from the $\mathrm{Cr_{adv}} = 2.5$ simulation is almost identical to the solution using $\mathrm{Cr_{adv}} = 0.56$.

The CSLAM-SW is numerically stable for the highly-nonlinear flow in the Gaussian jet and at Courant numbers much greater than unity. To check that consistency and shape-preservation in such a highly-divergent flow can be maintained, we repeat the Gaussian jet case using CSLAM-SW and the shape-preserving extensions described in section 3.

d. Gaussian jet – Ro = 5.0 with shape-preservation

The shape-preserving CSLAM-SW solver (19) is tested using the divergent flow of the Gaussian jet as described in section 4c. We also test the LKM solver with the Barth and Jespersen (1989) filter implemented in the explicit scalar transport scheme of hq_{exp}^{n+1}. All parameters are as described in section 4c, and a time step of $\Delta t = 100$ s is used for results in Figs. 10 and 11.

To test for numerical consistency in the two solvers, we repeat the consistency test described in section 4a by initializing a constant specific concentration field $q_0 = 1$. The shape-preserving CSLAM-SW solution is able to maintain numerical consistency between h and hq up to machine roundoff for this highly-divergent flow and the result is independent of time-step size. As for LKM, despite the shape-preserving transport scheme in the solver, numerical inconsistency is still an issue with a maximum absolute error (defined as the deviation from $q_0 = 1$) of 6.79×10^{-3}, a mean absolute error of 4.82×10^{-4}, and a root-mean-squared error of 1.06×10^{-3} at time $T = 1.8 \times 10^5$ s (Fig. 10), and as in section 4a, the error is a function of the time-step size (not shown).

To compare the shape-preservation ability between CSLAM-SW and LKM, we initialize a specific-concentration distribution that varies only in the x-direction and has a sharp gradient that coincides with the center of the initial jet:

$$q(x, y, t = 0) = \begin{cases} 1.0, & \text{if } -X/2 \leq x < 0. \\ 0.1, & \text{if } 0 \leq x < X/2. \end{cases}$$

Solutions of q diagnosed from hq from the non-shape-preserving CSLAM-SW, LKM with shape-preserving transport, and the shape-preserving CSLAM-SW are presented in Figs. 11a-c. The simulation time $T = 1.8 \times 10^5$ s in the figure corresponds to the vorticity field shown in Fig. 8.

For the non-shape-preserving CSLAM-SW solver (Fig. 11a), q reaches an unphysical peak value of 1.233 and an unphysical minimum value of -0.145 (specific concentrations cannot be negative). The LKM solver with shape-preserving transport (Fig. 11b) has less severe errors than the non-shape-preserving CSLAM-SW, but loses its shape-preserving ability due to numerical inconsistency. The minimum and maximum q values are 0.09997 and 1.0063 respectively at time $T = 1.8 \times 10^5$ s. The overshooting of q (which may generate spurious constituent mass) appears to be greater in amplitude than the undershooting for this flow. Overshooting occurs mostly within the strongest anticyclones (negative vorticity centers on the left side of the channel, highlighted in solid black lines in Fig. 11b). Using the shape-preserving CSLAM-SW solver (Fig. 11c), minimum and maximum values of q are kept within its physical limits (0.1 and 1.0 respectively, up to machine roundoff) and shape-preservation is ensured.

5. Conclusion

A conservative and consistent semi-Lagrangian semi-implicit solver is constructed and tested for shallow-water flows (CSLAM-SW). The model uses a new flux-form discretization of the semi-implicit cell-integrated semi-Lagrangian continuity equation that allows a straight-forward implementation of a consistent constituent transport scheme. Like typical conservative semi-Lagrangian semi-implicit schemes, the algorithm requires at each time step a single Helmholtz equation solution and a single application of CSLAM.

Specifically, our new discretization uses the flux divergence as opposed to a velocity divergence that requires linearization about a constant mean reference state. For traditional semi-implicit schemes, the dependence on a constant mean reference state makes it difficult to ensure consistency between total fluid mass and constituent mass. When numerical consistency is not maintained, constituent mass conservation can be violated even for solvers that use inherently-conservative transport schemes. More unacceptably, constituent fields may no longer preserve their shapes, e.g. losing constancy or positive-definiteness.

We have shown an example of a traditional discrete cell-integrated semi-Lagrangian semi-implicit continuity equation (LKM), in which inconsistency can generate significant numerical errors in the specific constituent concentration. The inconsistent semi-implicit correction term in LKM causes errors to grow proportionally with time step size and with the nonlinearity of the flow. The ideal radially-propagating gravity wave tests using the LKM solver showed a maximum absolute error in an initially constant specific concentration ($q_0 = 1$) field ranging from an order of 10^{-7} to 10^{-3} in the linear case, and an order of 10^{-4} to 10^{-1} in the nonlinear case. The orders of magnitude of these errors are significant relative to the specific concentration of tracers and water vapour in the atmosphere. The consistent formulation in the new CSLAM-SW on the other hand eliminates these errors (up to machine roundoff).

The new flux-form solver (CSLAM-SW) is tested for a range of flows and Courant numbers for the shallow-water system, and is stable and compares well with other existing semi-implicit schemes, including a two-time-level traditional semi-Lagrangian scheme and an Eulerian leap-frog scheme. The Gaussian jet test (the more nonlinear jet of the two presented) showed that CSLAM-SW remains numerically stable when large time steps are used.

We have also identified and eliminated a computational unstable mode in CSLAM-SW and LKM, using the discrete dispersion relation of the linearized shallow-water equations. The numerical instability, associated with the Lagrangian divergence operator on a C-grid, can be eliminated by introducing a new averaging operator on the Coriolis terms in the momentum equations.

Shape-preservation in CSLAM-SW is ensured by applying a 2D shape-preserving filter in the CSLAM transport scheme and the first-order upwind scheme to compute the predictor-corrector and flux-form correction terms. As shown in the Gaussian jet case, without any shape-preserving filter, unphysical negative and unreasonable positive specific concentrations may develop due to undershoots and overshoots. For inconsistent formulations such as that in LKM, the use of a shape-preserving explicit transport scheme cannot guarantee shape-preservation either due to numerical consistency errors. CSLAM-SW, on the other hand, allows for straightforward implementation of existing shape-preserving schemes and filters and ensures shape-preservation (up to machine roundoff).

The initial testing of the semi-implicit formulation in CSLAM-SW shows promising results. We are currently implementing the extension of CSLAM-SW to a 2D (x-z) non-hydrostatic, fully-compressible atmospheric solver. The desirable properties of mass conservation, consistency, and shape-preservation for moisture variables and tracers will likely be important for both short- and long-term meteorological applications.

Acknowledgments.

This work was done as a part of the National Center for Atmospheric Research - Graduate Visitor Advanced Study Program. The authors thank Joseph Klemp for his suggestions on the dispersion relation analysis of CSLAM-SW. The first author would also like to acknowledge the Canadian Natural Science and Engineering Research Council for their financial support via the Discovery Grant to the last author.

APPENDIX

Numerical schemes for comparison

a. A two-time-level traditional semi-Lagrangian semi-implicit model

A traditional grid-point semi-implicit semi-Lagrangian model on a staggered C-grid is constructed for comparison purposes. The scheme uses a forward-in-time off-centering parameter β for numerical stability purposes. The discretized system is given by

$$u_A^{n+1} = \Delta t\Big(\frac{1+\beta}{2}\Big)\Big[f\overline{v}^{xy} - g'\delta_x h\Big]_A^{n+1} + R_u^n, \tag{A1}$$

$$v_A^{n+1} = \Delta t\Big(\frac{1+\beta}{2}\Big)\Big[-f\overline{u}^{xy} - g'\delta_y h\Big]_A^{n+1} + R_v^n, \tag{A2}$$

$$h_A^{n+1} = -\Delta t\Big(\frac{1+\beta}{2}\Big)H_0\Big(\delta_x u + \delta_y v\Big)_A^{n+1} + R_h^n + R_h^{n+\frac{1}{2}},$$

where

$$R_u^n = u_d^n + \Delta t\Big(\frac{1-\beta}{2}\Big)\Big[f\overline{v}^{xy} - g'\delta_x h\Big]_d^n,$$

$$R_v^n = v_d^n + \Delta t\Big(\frac{1-\beta}{2}\Big)\Big[-f\overline{u}^{xy} - g'\delta_y h\Big]_d^n,$$

$$R_h^n = h_d^n - \Delta t\Big(\frac{1-\beta}{2}\Big)H_0\Big(\delta_x u + \delta_y v\Big)_d^n,$$

$$R_h^{n+\frac{1}{2}} = -\Delta t\Big(h'\delta_x u + h'\delta_y v\Big)_{d/2}^{n+\frac{1}{2}},$$

and $h' = h - H_0$. The operators are defined as

$$\delta_x\phi = \frac{\phi_{i,j} - \phi_{i-1,j}}{\Delta x};\quad \delta_y\phi = \frac{\phi_{i,j} - \phi_{i,j-1}}{\Delta y},$$

$$\overline{\phi}^x = \frac{1}{2}(\phi_{i,j} + \phi_{i+1,j}),$$

$$\overline{\phi}^{xy} = \overline{\overline{\phi}^x}^y = \overline{\overline{\phi}^y}^x = \frac{1}{4}(\phi_{i,j} + \phi_{i,j+1} + \phi_{i+1,j} + \phi_{i+1,j+1}).$$

The R^n terms define the known terms that are evaluated at time level n and interpolated to the departure point. The $R^{n+\frac{1}{2}}$ term is the nonlinear term evaluated by extrapolating values from time level n and $n-1$ to time level $n+\frac{1}{2}$, and interpolated to the estimated mid-point trajectory. The time-off-centering parameter β is set to 0.1 for all runs.

b. *An Eulerian leap-frog semi-implicit advective model*

The Eulerian C-grid staggering model uses the semi-implicit leap-frog time-stepping scheme and momentum equations in the advective form. The model has an Asselin time-filter and a time-off-centering parameter ($\beta = 0.1$) to eliminate spurious oscillations. Numerical viscosity is also applied for certain test cases (see section 4b). Using the same notations as for the traditional semi-Lagrangian model, the discretized system is given by

$$u^{n+1} = \Delta t\big(1+\beta\big)\Big(f\overline{v}^{xy} - g\delta_x h\Big)^{n+1} + R_u,$$

$$v^{n+1} = \Delta t\big(1+\beta\big)\Big(-f\overline{u}^{xy} - g\delta_y h\Big)^{n+1} + R_v,$$

$$h^{n+1} = -\Delta t\big(1+\beta\big)H_0\Big(\delta_x u + \delta_y v\Big)^{n+1} + R_h,$$

where

$$R_u = u^{n-1} - 2\Delta t\Big(u\delta_x u + v\delta_y u\Big)^{n} + \Delta t(1-\beta)\Big(f\overline{v}^{xy} - g\delta_x h\Big)^{n-1},$$

$$R_v = v^{n-1} - 2\Delta t\Big(u\delta_x v + v\delta_y v\Big)^{n} + \Delta t\big(1-\beta\big)\Big(-f\overline{u}^{xy} - g\delta_y h\Big)^{n-1},$$

$$R_h = h^{n-1} - \Delta t\big(1-\beta\big)H_0\Big(\delta_x u + \delta_y v\Big)^{n-1} - 2\Delta t\Big(h'\delta_x u + h'\delta_y v\Big)^{n+\frac{1}{2}}.$$

REFERENCES

Barth, T. J. and D. C. Jespersen, 1989: The design and application of upwind schemes on unstructured meshes. *27th Aerospace Sciences Meeting*, **89 (89-0366)**.

Durran, D. R., 2010: *Numerical Methods for Fluid Dynamics – With Applications to Geophysics*. 2d ed., Springer, 516 pp.

Jöckel, P., R. von Kuhlmann, M. Lawrence, B. Steil, C. Brenninkmeijer, P. Crutzen, P. Rasch, and B. Eaton, 2001: On a fundamental problem in implementing flux-form advection schemes for tracer transport in 3-dimensional general circulation and chemistry transport models. *Q. J. R. Meteorol. Soc.*, **127**, 1035–1052.

Kwizak, M. and A. Robert, 1971: A semi-implicit scheme for grid point atmospheric models of the primitive equations. *Mon. Wea. Rev.*, **99**, 32–36.

Laprise, J. and A. Plante, 1995: A class of semi-Lagrangian integrated-mass (SLIM) numerical transport algorithms. *Mon. Wea. Rev.*, **123**, 553–565.

Lauritzen, P. H., 2005: An Inherently Mass-conservative Semi-implicit Semi-lagrangian Model. Ph.D. thesis, University of Copenhagen, Denmark, 283 pp., [Available from http://www.cgd.ucar.edu/cms/pel/papers/phd.pdf.].

Lauritzen, P. H., E. Kaas, and B. Machenhauer, 2006: A mass-conservative semi-implicit semi-Lagrangian limited-area shallow-water model on the sphere. *Mon. Wea. Rev.*, **134**, 1205–1221.

Lauritzen, P. H., E. Kaas, B. Machenhauer, and K. Lindberg, 2008: A mass-conservative version of the semi-implicit semi-Lagrangian HIRLAM. *Q. J. R. Meteorol. Soc.*, **134**, 1583–1595.

Lauritzen, P. H., R. D. Nair, and P. A. Ullrich, 2010: A conservative semi-Lagrangian multi-tracer transport scheme (CSLAM) on the cubed-sphere grid. *J. Comput. Phys.*, **229**, 1401–1424.

Machenhauer, B., E. Kaas, and P. H. Lauritzen, 2009: Finite volume meteorology. *Computational Methods for the Atmosphere and the Oceans: Special Volume*, R. Temam and J. Tribbia, Eds., Elsevier, Handb. Numer. Anal., 3–120.

Machenhauer, B. and M. Olk, 1997: The implementation of the semi-implicit scheme in cell-integrated semi-Lagrangian models. *Atmos.-Ocean*, **35 (special issue)**, 103–126.

Nair, R. and B. Machenhauer, 2002: The mass-conservative cell-integrated semi-Lagrangian advection scheme on the sphere. *Mon. Wea. Rev.*, **130**, 649–667.

Nair, R. D. and P. H. Lauritzen, 2010: A class of deformational flow test cases for linear transport problems on the sphere. *J. Comput. Phys.*, **229**, 8868–8887.

Poulin, F. and G. Flierl, 2003: The nonlinear evolution of barotropically unstable jets. *J. Phys. Oceanogr.*, **33**, 2173–2192.

Rancic, M., 1992: Semi-Lagrangian piecewise biparabolic scheme for two-dimensional horizontal advection of a passive scalar. *Mon. Wea. Rev.*, **120**, 1394–1406.

Randall, D., 1994: Geostrophic adjustment and the finite-difference shallow-water equations. *Mon. Wea. Rev.*, **122**, 1371–1377.

Rasch, P. and D. Williamson, 1990: Computational aspects of moisture transport in global-models of the atmosphere. *Q. J. R. Meteorol. Soc.*, **116**, 1071–1090.

Robert, A., 1981: A stable numerical integration scheme for the primitive meteorological equations. *Atmos.-Ocean*, **19**, 35–46.

Robert, A., T. Yee, and H. Ritchie, 1985: A semi-Lagrangian and semi-implicit numerical-integration scheme for multilevel atmospheric models. *Mon. Wea. Rev.*, **113**, 388–394.

Thuburn, J., 2008: A fully implicit, mass-conserving, semi-Lagrangian scheme for the f-plane shallow-water equations. *Int. J. Numer. Methods Fluids*, **56**, 1047–1059.

Thuburn, J., M. Zerroukat, N. Wood, and A. Staniforth, 2010: Coupling a mass-conserving semi-Lagrangian scheme (SLICE) to a semi-implicit discretization of the shallow-water equations: Minimizing the dependence on a reference atmosphere. *Q. J. R. Meteorol. Soc.*, **136**, 146–154.

Zerroukat, M., N. Wood, and A. Staniforth, 2002: SLICE: A semi-Lagrangian inherently conserving and efficient scheme for transport problems. *Q. J. R. Meteorol. Soc.*, **128**, 2801–2820.

Zhang, K., H. Wan, B. Wang, and M. Zhang, 2008: Consistency problem with tracer advection in the atmospheric model GAMIL. *Adv. Atmos. Sci.*, **25**, 306–318.

List of Figures

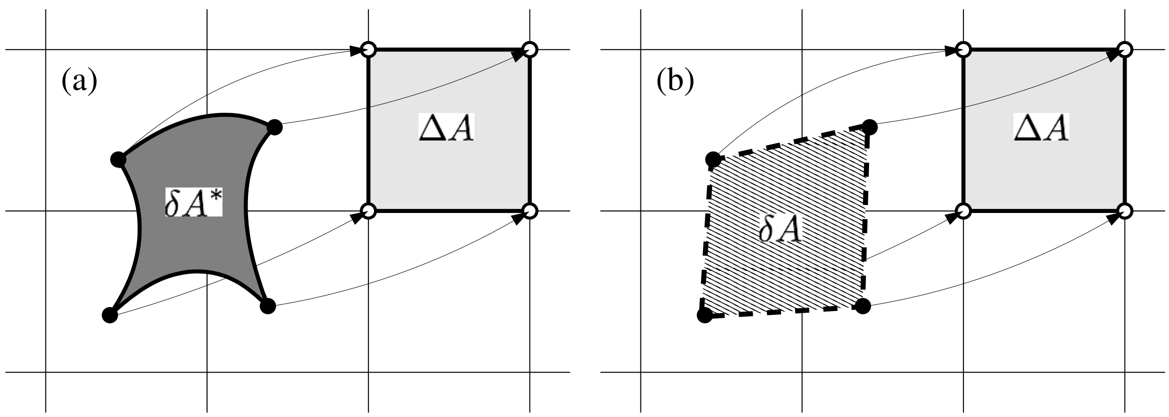

Fig. 1. (a) Exact departure cell area (δA^*, dark grey region) and the corresponding arrival grid cell (ΔA, light grey region). (b) Departure cells in CSLAM (δA) are represented as polygons defined by the departure locations of the arrival grid cell vertices.

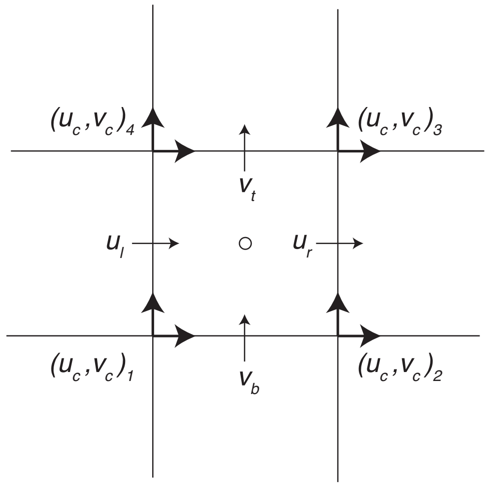

FIG. 2. Definition of an Eulerian arrival grid cell, and its associated velocities at the cell faces (u_l, u_r, v_t, v_b) and cell corners $(u_c, v_c)_i$ for i=1, 2, 3, 4.

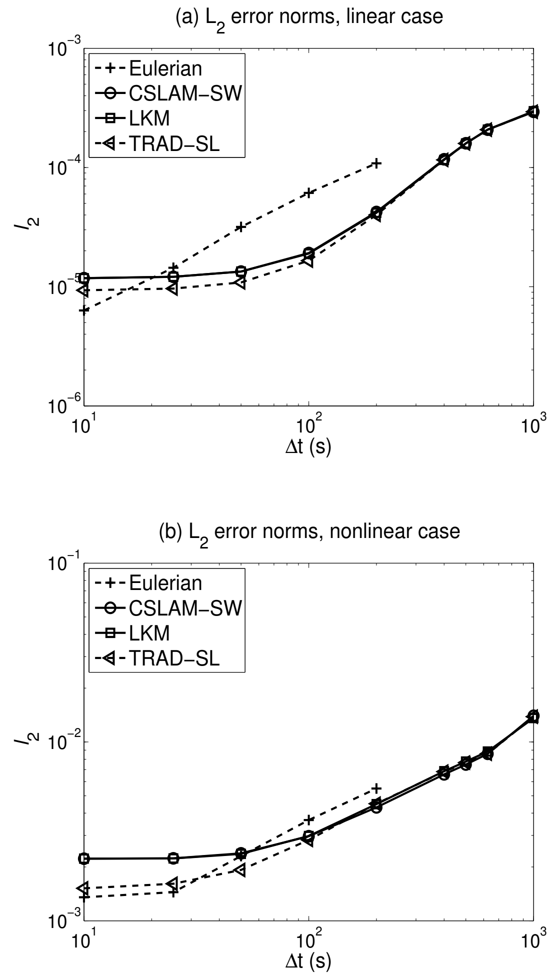

FIG. 3. Comparison of the height field L_2 error norms for the radially-propagating gravity-wave solutions. Errors are plotted at time $T = 1 \times 10^5$ s for the (a) linear ($\Delta h = 10$ m and $h_0 = 990$ m) and (b) non-linear ($\Delta h = 500$ m and $h_0 = 1000$ m) test cases computed on a 500 m mesh. Note the different scales in the plots.

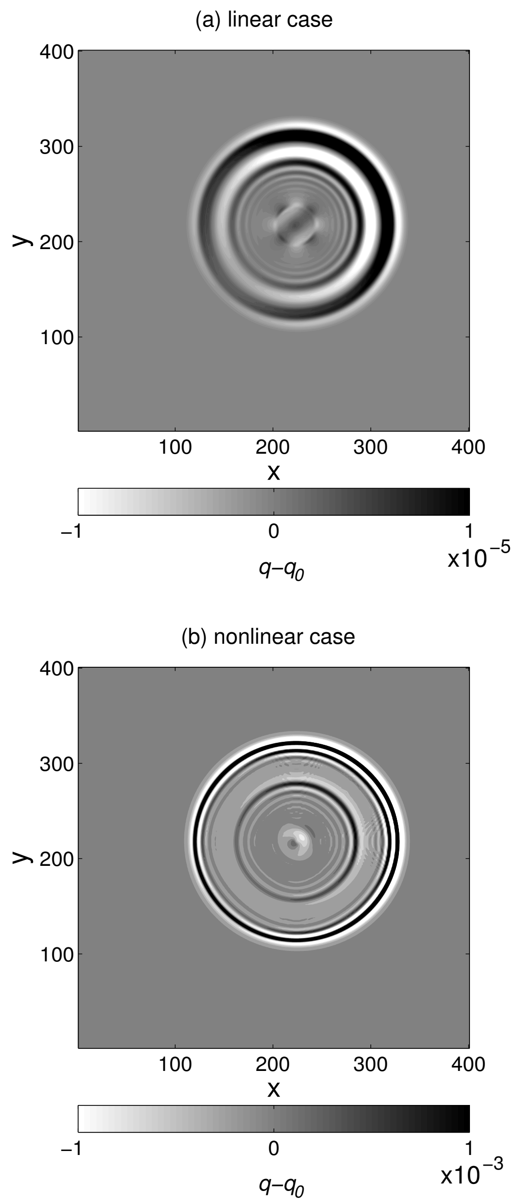

FIG. 4. Specific concentration error $(q - q_0)$ in LKM for a divergent flow initialized with a constant $q_0 = 1$ in the (a) linear ($\Delta h = 10$ m and $h_0 = 990$ m) and (b) nonlinear ($\Delta h = 500$ m and $h_0 = 1000$ m) height perturbation cases. Note the different scales in the plots.

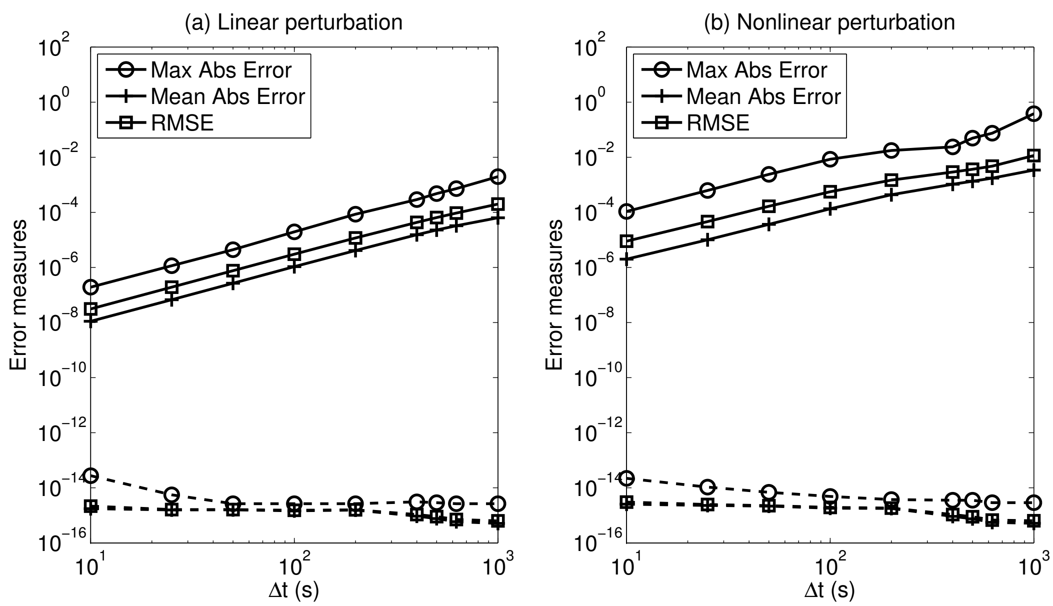

FIG. 5. Variation of specific concentration error $(q - q_0)$ (maximum absolute error, mean absolute error, and root-mean-squared error) with time step size in LKM (solid line) and CSLAM-SW (dashed line) for the (a) linear height perturbation and (b) nonlinear height perturbation cases.

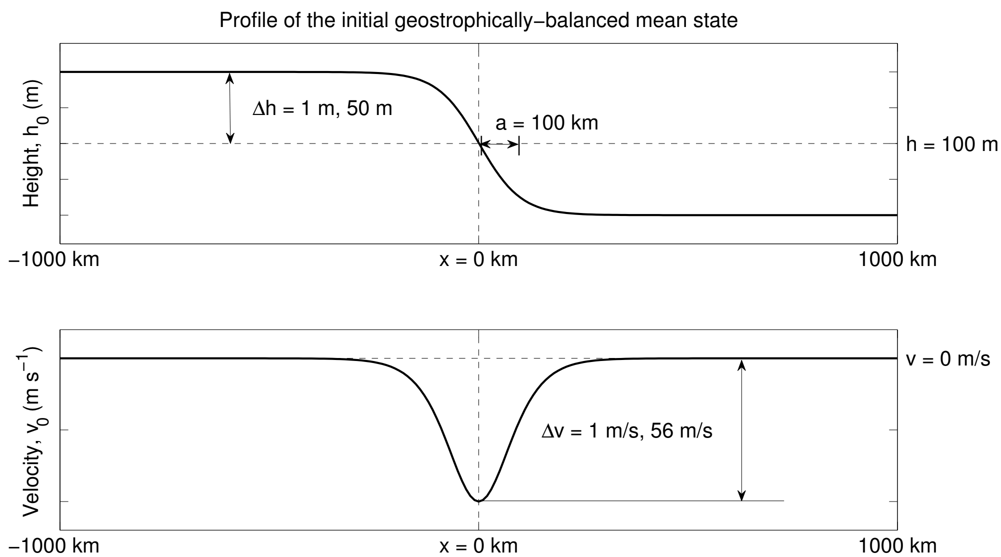

FIG. 6. Initial mean height h_0 (top) and velocity v_0 (bottom) profiles for the Bickley jet ($\Delta h = 1$ m, $\Delta v = 1$ m s^{-1}) and Gaussian jet ($\Delta h = 50$ m, $\Delta v = 56$ m s^{-1}).

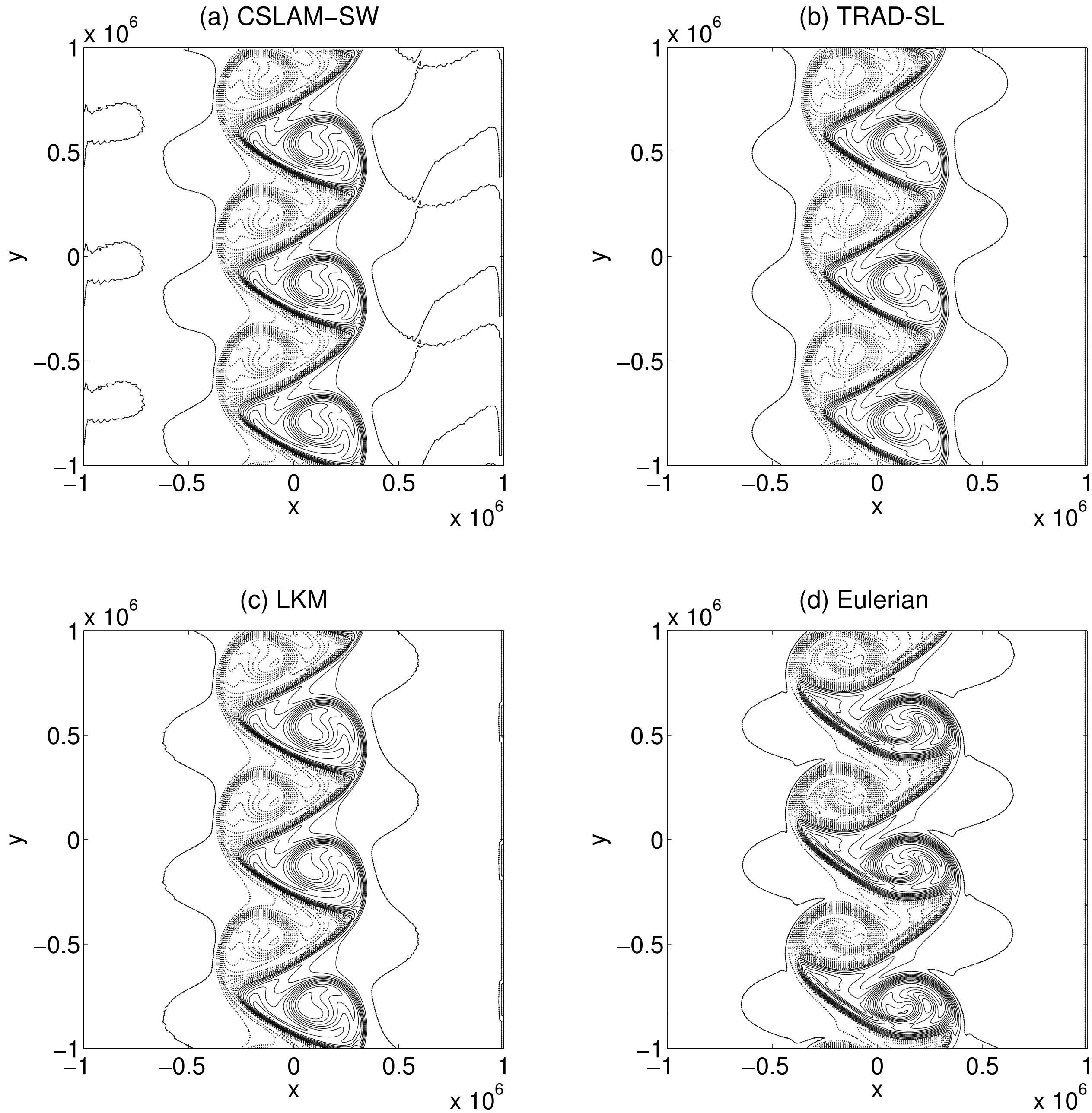

FIG. 7. Solutions of the Bickley jet at time $T = 5 \times 10^6$ s (after 2500 time steps) for Ro = 0.1, Fr = 0.1 and $\mathrm{Cr}_{\mathrm{adv}} = 0.2$. Plotted are positive (solid line) and negative (dashed line) vorticity between -1×10^{-5} s^{-1} and 1×10^{-5} s^{-1} with a contour interval of 5×10^{-7} s^{-1}.

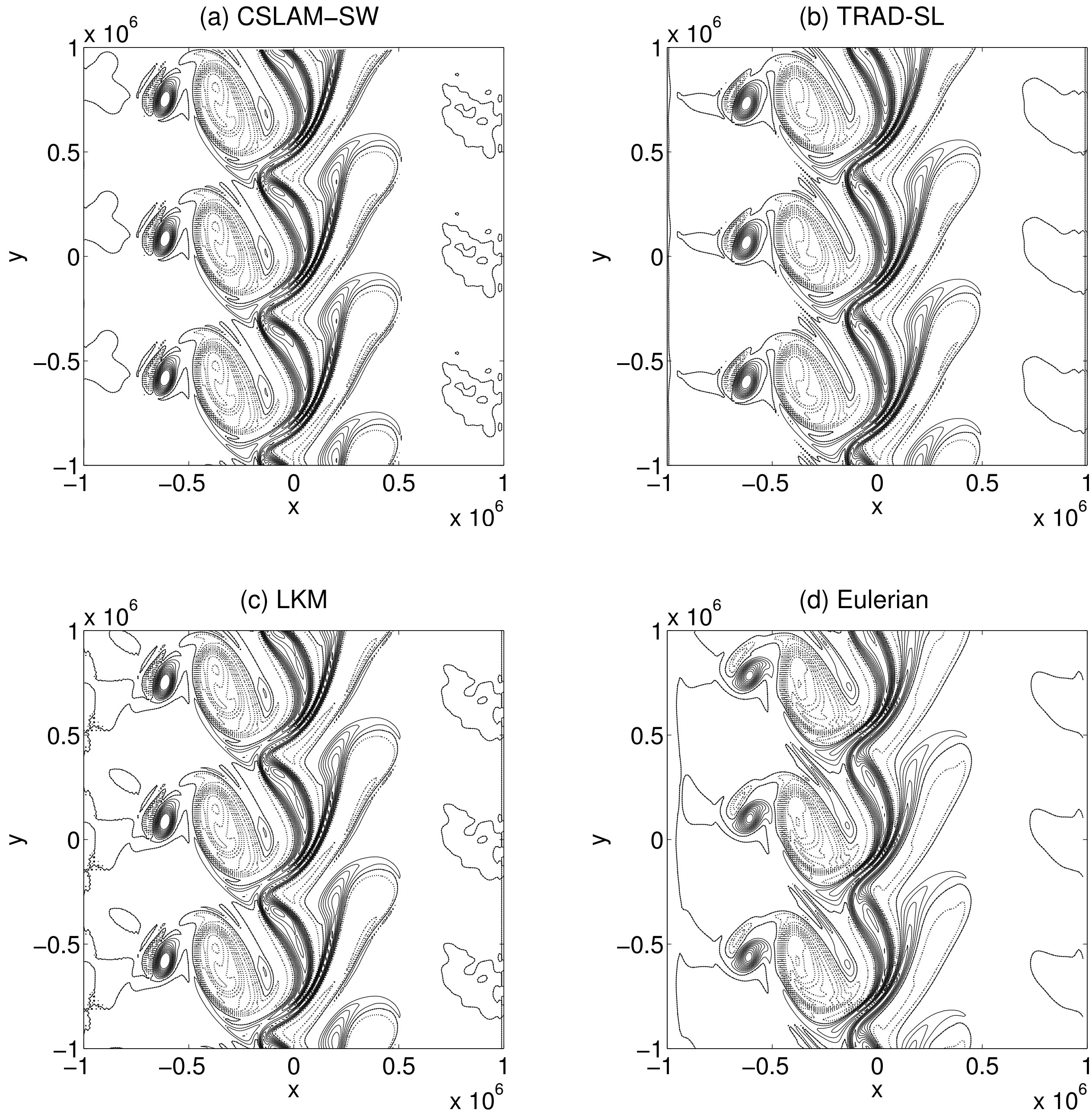

FIG. 8. Solutions of the Gaussian jet for $\mathrm{Ro} = 5.0$ and $\mathrm{Cr}_{\mathrm{adv}} = 0.56$ at time $T = 1.8 \times 10^5$ s (after 1800 time steps). Plotted are positive (solid line) and negative (dashed line) vorticity between -5×10^{-4} s^{-1} and 5×10^{-4} s^{-1} with a contour interval of 5×10^{-5} s^{-1}.

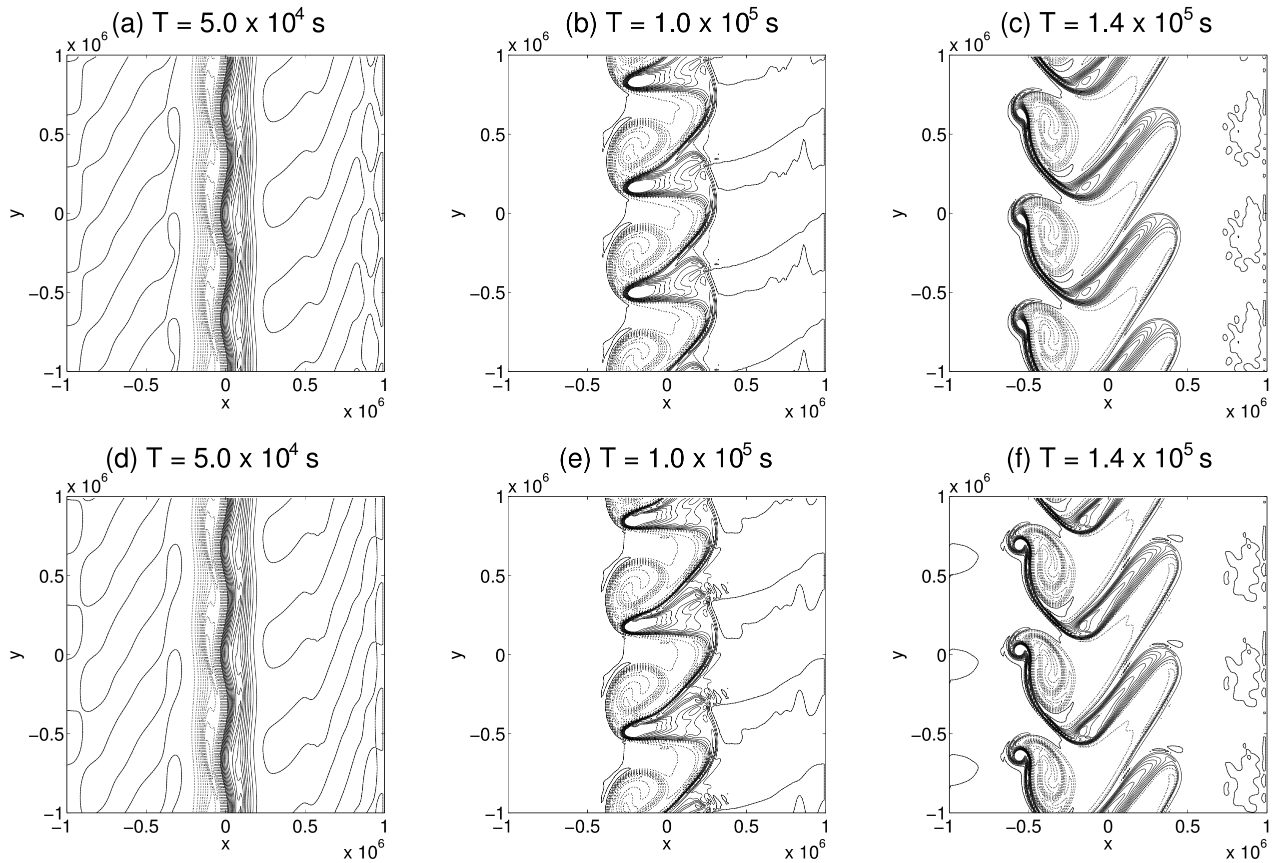

FIG. 9. CSLAM-SW solutions of the Gaussian jet for Ro = 5.0 at three different times (left to right on each row) of the simulation: at time $T = 5 \times 10^4$ s, 1.0×10^5 s, and 1.4×10^5 s. (a - c) Solutions using a $\mathrm{Cr_{adv}}$ of 0.56 (same simulation as in Fig. 8) (d - f) Solutions using a larger $\mathrm{Cr_{adv}}$ of 2.5. Plotted are positive (solid line) and negative (dashed line) vorticity between -5×10^{-4} s^{-1} and 5×10^{-4} s^{-1} with a contour interval of 5×10^{-5} s^{-1}.

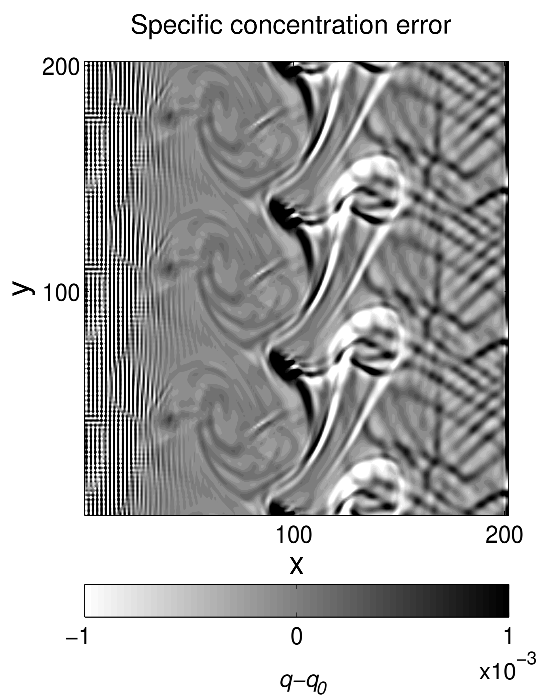

FIG. 10. Specific concentration error $(q - q_0)$ in LKM for the Gaussian jet at time $T = 1.8 \times 10^5$ s, initialized with a constant $q_0 = 1$ field.

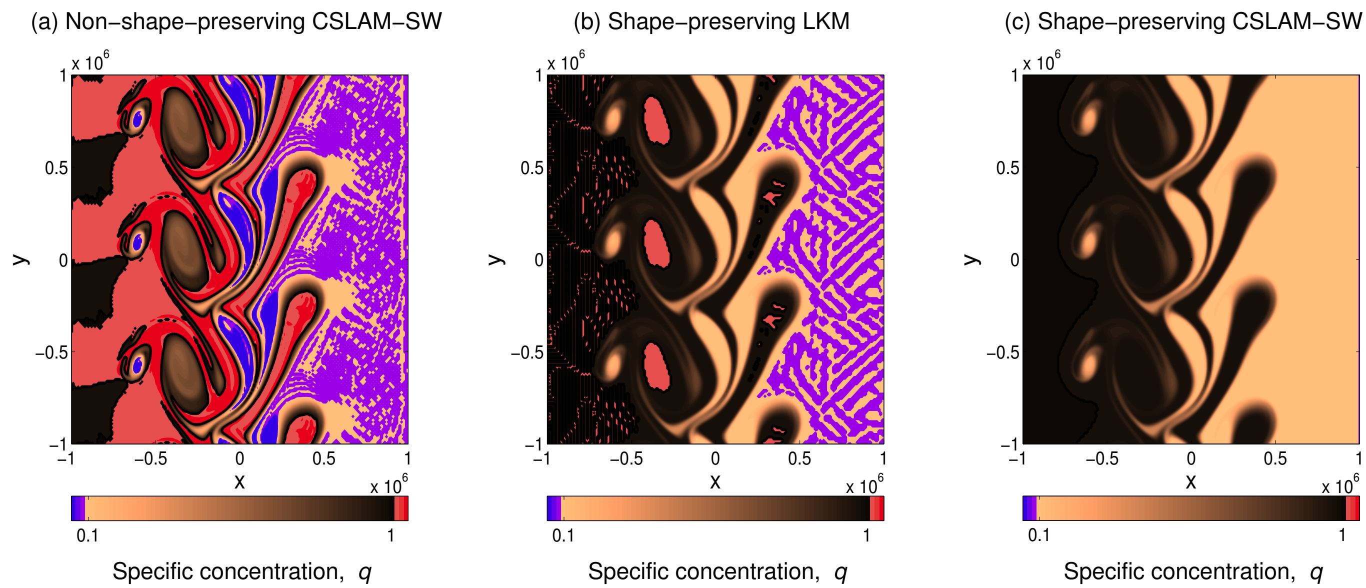

Fig. 11. Specific constituent concentration q at time $T = 1.8 \times 10^5$ s. Initial minimum and maximum q are 0.1 and 1.0 respectively. Regions with unphysical overshooting (red) and undershooting (purple) are highlighted.